Swarthmore College
Works

Physics & Astronomy Faculty Works   Physics & Astronomy

9-1-2015

KELT-8b: A Highly Inflated Transiting Hot Jupiter And A New Technique For Extracting High-Precision Radial Velocities From Noisy Spectra

B. J. Fulton

K. A. Collins

B. S. Gaudi

K. G. Stassun

J. Pepper

See next page for additional authors

Follow this and additional works at: http://works.swarthmore.edu/fac-physics

Part of the Astrophysics and Astronomy Commons

Recommended Citation

B. J. Fulton, K. A. Collins, B. S. Gaudi, K. G. Stassun, J. Pepper, T. G. Beatty, R. J. Siverd, K. Penev, A. W. Howard, C. Baranec, G. Corfini, J. D. Eastman, J. Gregorio, N. M. Law, M. B. Lund, T. E. Oberst, M. T. Penny, R. Riddle, J. E. Rodriguez, D. J. Stevens, R. Zambelli, C. Ziegler, A. Bieryla, G. D'Ago, D. L. DePoy, Eric L.N. Jensen, J. F. Kielkopf, D. W. Latham, M. Manner, J. Marshall, K. K. McLeod, and P. A. Reed. (2015). "KELT-8b: A Highly Inflated Transiting Hot Jupiter And A New Technique For Extracting High-Precision Radial Velocities From Noisy Spectra". *Astrophysical Journal*. Volume 810, Issue 1.
http://works.swarthmore.edu/fac-physics/254

Authors

B. J. Fulton, K. A. Collins, B. S. Gaudi, K. G. Stassun, J. Pepper, T. G. Beatty, R. J. Siverd, K. Penev, A. W. Howard, C. Baranec, G. Corfini, J. D. Eastman, J. Gregorio, N. M. Law, M. B. Lund, T. E. Oberst, M. T. Penny, R. Riddle, J. E. Rodriguez, D. J. Stevens, R. Zambelli, C. Ziegler, A. Bieryla, G. D'Ago, D. L. DePoy, Eric L.N. Jensen, J. F. Kielkopf, D. W. Latham, M. Manner, J. Marshall, K. K. McLeod, and P. A. Reed

KELT-8b: A HIGHLY INFLATED TRANSITING HOT JUPITER AND A NEW TECHNIQUE FOR EXTRACTING HIGH-PRECISION RADIAL VELOCITIES FROM NOISY SPECTRA

BENJAMIN J. FULTON[1,22], KAREN A. COLLINS[2,3], B. SCOTT GAUDI[4], KEIVAN G. STASSUN[3,5], JOSHUA PEPPER[3,6],
THOMAS G. BEATTY[7], ROBERT J. SIVERD[8], KALOYAN PENEV[9], ANDREW W. HOWARD[1], CHRISTOPH BARANEC[1], GIORGIO CORFINI[10],
JASON D. EASTMAN[11], JOAO GREGORIO[12], NICHOLAS M. LAW[13], MICHAEL B. LUND[6], THOMAS E. OBERST[14],
MATTHEW T. PENNY[4,23], REED RIDDLE[15], JOSEPH E. RODRIGUEZ[6], DANIEL J. STEVENS[4], ROBERTO ZAMBELLI[10], CARL ZIEGLER[13],
ALLYSON BIERYLA[11], GIUSEPPE D'AGO[16], DARREN L. DEPOY[17], ERIC L. N. JENSEN[18], JOHN F. KIELKOPF[2], DAVID W. LATHAM[11],
MARK MANNER[19], JENNIFER MARSHALL[17], KIM K. MCLEOD[20], AND PHILLIP A. REED[21]

[1] Institute for Astronomy, University of Hawai'i, 2680 Woodlawn Drive, Honolulu, HI 96822, USA; bfulton@hawaii.edu
[2] Department of Physics and Astronomy, University of Louisville, Louisville, KY 40292, USA
[3] Department of Physics and Astronomy, Vanderbilt University, Nashville, TN 37235, USA
[4] Department of Astronomy, The Ohio State University, 140 West 18th Avenue, Columbus, OH 43210, USA
[5] Department of Physics, Fisk University, Nashville, TN 37208, USA
[6] Department of Physics, Lehigh University, Bethlehem, PA 18015, USA
[7] Department of Astronomy and Astrophysics and Center for Exoplanets and Habitable Worlds, The Pennsylvania State University, University Park, PA 16802, USA
[8] Las Cumbres Observatory Global Telescope Network, 6740 Cortona Drive, Suite 102, Santa Barbara, CA 93117, USA
[9] Department of Astrophysical Sciences, Princeton University, Princeton, NJ 08544, USA
[10] Societ Astronomica Lunae, Castelnuovo Magra I-19030, Via Montefrancio, 77—Italy
[11] Harvard-Smithsonian Center for Astrophysics, Cambridge, MA 02138 USA
[12] Atalaia Group and Crow-Observatory, Portalegre, Portugal
[13] Department of Physics and Astronomy, University of North Carolina at Chapel Hill, Chapel Hill, NC 27599, USA
[14] Department of Physics, Westminster College, New Wilmington, PA 16172, USA
[15] Division of Physics, Mathematics, and Astronomy, California Institute of Technology, Pasadena, CA 91125, USA
[16] Istituto Internazionale per gli Alti Studi Scientifici (IIASS), Via G. Pellegrino 19, I-84019, Vietri Sul Mare (SA), Italy
[17] George P. and Cynthia Woods Mitchell Institute for Fundamental Physics and Astronomy, Texas A and M University, College Station, TX 77843-4242, USA
[18] Department of Physics and Astronomy, Swarthmore Colleg, Swarthmore, PA 19081, USA
[19] Spot Observatory, Nunnelly, TN 37137, USA
[20] Wellesley College, Wellesley, MA 02481, USA
[21] Department of Physical Sciences, Kutztown University, Kutztown, PA 19530, USA

ABSTRACT

We announce the discovery of a highly inflated transiting hot Jupiter by the KELT-North survey. A global analysis including constraints from isochrones indicates that the $V = 10.8$ host star (HD 343246) is a mildly evolved, G dwarf with $T_{eff} = 5754^{+54}_{-55}$ K, $\log g = 4.078^{+0.049}_{-0.054}$, [Fe/H] $= 0.272 \pm 0.038$, an inferred mass $M_* = 1.211^{+0.078}_{-0.066}\,M_\odot$, and radius $R_* = 1.67^{+0.14}_{-0.12}\,R_\odot$. The planetary companion has a mass $M_P = 0.867^{+0.065}_{-0.061}\,M_J$, radius $R_P = 1.86^{+0.18}_{-0.16}\,R_J$, surface gravity $\log g_P = 2.793^{+0.072}_{-0.075}$, and density $\rho_P = 0.167^{+0.047}_{-0.038}$ g cm^{-3}. The planet is on a roughly circular orbit with semimajor axis $a = 0.04571^{+0.00096}_{-0.00084}$ AU and eccentricity $e = 0.035^{+0.050}_{-0.025}$. The best-fit linear ephemeris is $T_0 = 2456883.4803 \pm 0.0007$ BJD$_{TDB}$ and $P = 3.24406 \pm 0.00016$ days. This planet is one of the most inflated of all known transiting exoplanets, making it one of the few members of a class of extremely low density, highly irradiated gas giants. The low stellar $\log g$ and large implied radius are supported by stellar density constraints from follow-up light curves, as well as an evolutionary and space motion analysis. We also develop a new technique to extract high-precision radial velocities from noisy spectra that reduces the observing time needed to confirm transiting planet candidates. This planet boasts deep transits of a bright star, a large inferred atmospheric scale height, and a high equilibrium temperature of $T_{eq} = 1675^{+61}_{-55}$ K, assuming zero albedo and perfect heat redistribution, making it one of the best targets for future atmospheric characterization studies.

Key words: planetary systems – stars: individual (HD 343246)

1. INTRODUCTION

Ground-based surveys for transiting exoplanets have been extraordinarily successful in detecting Jupiter-size planets orbiting very close to their host stars (hot Jupiters). These planets are some of the easiest to detect and characterize, but also some of the most intrinsically rare, occurring around only 0.3%–1.5% of Sun-like stars (Gould et al. 2006; Cumming et al. 2008; Bayliss & Sackett 2011; Howard et al. 2012; Wright et al. 2012). Both radial velocity (RV) surveys and transit surveys are heavily biased to detect these massive close-in objects, yet we still know of only 162 examples of hot Jupiters out of the thousands of currently known exoplanets.[24]

Due to their short orbital periods and large transit and/or RV signals, these planets make excellent laboratories to study planet formation and migration theories (Ida & Lin 2008; Mordasini et al. 2009; Hansen & Murray 2012), atmospheric properties and composition (Lockwood et al. 2014; Zhao et al. 2014; Sing et al. 2015), and even the rotational velocities of giant planets (Snellen et al. 2014). Several mysteries remain

---

[22] NSF Graduate Research Fellow.
[23] Sagan Fellow.

[24] Planets with orbital periods shorter than 10 days and $M \sin i \geqslant 0.5\,M_J$ based on a 2015 March 3 query of exoplanets.org.

unsolved for this population of exoplanets, however, including the differences between the orbital distance distribution of close-in Jupiters orbiting metal-rich and metal-poor stars (Dawson & Murray-Clay 2013), the frequency of long-period companions in hot Jupiter systems (Knutson et al. 2014; Ngo et al. 2015), the source of large misalignments between the orbital axis and stellar spin axis (Albrecht et al. 2012; Dawson 2014), and the reason that many hot Jupiters are inflated to extremely large radii (Batygin et al. 2011; Ginzburg & Sari 2015). Each hot Jupiter discovery enhances our ability to explore these phenomena and study individual systems in exquisite detail.

RV surveys have discovered many non-transiting hot Jupiters around very bright stars, while the target stars of transit surveys tend to be much fainter. This is primarily due to the fact that only a narrow range of orbital parameters cause a planet to transit and many tens of thousands of stars must be observed in order to detect a single transiting planet. Because bright stars are distributed across a large area of the sky, it is generally more efficient to observe small areas of the sky to a greater depth for transits of fainter stars. The Kilodegree Extremely Little Telescope survey (KELT, Pepper et al. 2007) serves to bridge the gap in host star brightness between RV-detected and transit-detected planets by using extremely small aperture telescopes with large fields of view to observe nearly the entire sky. The survey is optimized to detect planets orbiting stars with V-band magnitudes between 8 and 10, but it has also been successful in detecting planets around slightly fainter stars (Collins et al. 2014).

We report the discovery of a highly inflated ($R_p = 1.86^{+0.18}_{-0.16}$ R_J, $M_p = 0.867^{+0.065}_{-0.061}$ M_J) hot Jupiter orbiting the moderately bright $V = 10.84$ G dwarf; HD 343246 (KELT-8 hereafter). KELT-8b has the second largest radius and seventh lowest density among all transiting exoplanets, with only WASP-17b being larger (Southworth et al. 2012; Bento et al. 2014). The planet lies well above the Seager et al. (2007) mass–radius relation for a pure hydrogen composition. In order to facilitate rapid and efficient RV confirmation of the planet, we developed a new technique that saves significant telescope resources when collecting RV measurements using the iodine technique (Butler et al. 1996). In Section 2 we describe our discovery and follow-up observations. We describe our spectroscopic analysis of the host star and summarize the inferred stellar properties in Section 3. A close companion stellar object that was ultimately found to be a background contaminant is described in Section 3.4. We outline our new technique for RV extraction in Section 4. A global analysis of the photometric and RV data is presented in Section 5, and we conclude with a discussion in Section 6 and summary in Section 7.

2. OBSERVATIONS

2.1. KELT Photometry

The KELT-North survey telescope consists of an Apogee AP16E imager (4 K × 4 K CCD with 9 μm pixels) and an 80 mm Mamiya 645 camera lens (42 mm diameter, $f/1.9$) behind a Kodak Wratten #8 red-pass filter. This setup achieves a 26° × 26° field of view with roughly 23″ pixel^{-1}. For a more complete description of the hardware and operations, see Pepper et al. (2007).

Raw KELT science images are dark-subtracted and flat-fielded using standard methods and then reduced using a heavily modified implementation of the ISIS image subtraction package (Alard & Lupton 1998; Alard 2000) coupled with our own high-performance background-removal routines. Stars are identified for extraction using the standalone DAOPHOT II PSF-fitting software package (Stetson 1987, 1990). To reduce systematic errors, extracted light curves are processed with the trend filtering algorithm (Kovács et al. 2005) prior to period search. A more complete description of the data reduction pipeline and candidate selection process are available in Siverd et al. (2012).

KELT-8 resides in KELT-North field 11, centered on ($\alpha = 19^h26^m48^s$, $\delta = +31°39′56″$; J2000). The data set consists of 5978 images acquired between 2007 May 30 and 2013 June 14. The full discovery light curve, phased to the KELT-8b transit ephemeris, is shown in Figure 1.

2.2. Follow-up Photometry

We acquired follow-up time series photometry of KELT-8 to better determine the transit shape and to check for a consistent transit depth across the optical filter bands. To schedule follow-up photometry, we used the `Tapir` software package (Jensen 2013). We obtained full primary transits in multiple bands between 2014 July and 2014 September. Figure 2 shows all the primary transit follow-up light curves assembled. A summary of the follow-up photometric observations is shown in Table 1. We find consistent $R_P/R_\star$ ratios in the g', r', i', V, and I_C filters after compensating for blending with a nearby neighbor in some observations (see below), helping to rule out false positives due to blended eclipsing binaries. The lower panel of Figure 2 shows all primary transit follow-up light curves from Figure 2, combined and binned in 5 minute intervals. This combined and binned light curve is not used for analysis, but rather to show the overall statistical power of the follow-up photometry.

AstroImageJ[25] (AIJ; K. A. Collins & J. F. Kielkopf 2015, in preparation) was used to calculate the differential photometric data from all calibrated image sequences. AIJ is a general purpose image processing package, but is optimized for processing time series astronomical image sequences.

2.2.1. MORC

We observed one complete KELT-8b transit on UT 2014-08-04 from the 0.6 m Moore Observatory RCOS (MORC) telescope, operated by the University of Louisville. MORC is equipped with an Apogee U16M 4 K × 4 K CCD giving a 26′ × 26′ field of view and 0.39 arcsec pixel^{-1}. The transit was observed pseudo-simultaneously in two filters by alternating between the g' and i' filters from one exposure to the next. The filter change is made during CCD read-out to minimize loss of time on the the sky. Since KELT-8b has a nearby neighbor, telescope defocusing was minimal to provide better separation of the flux from the two stars on the detector.

2.2.2. GCorfini

We observed one full transit on UT 2014-07-31 from Giorgio Corfini's home observatory (GCorfini) in Lucca, Italy. The observations were obtained in the V band using a 0.2 m
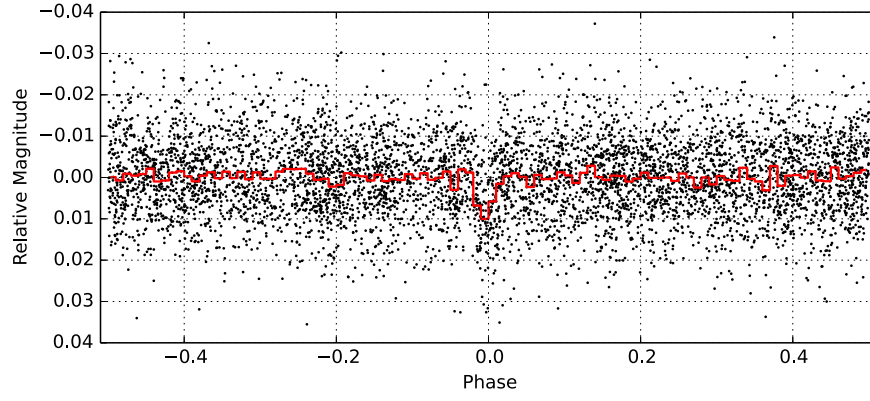

Figure 1. Discovery light curve of KELT-8b from the KELT-North telescope. The photometry is phase-folded to the ephemeris listed in Table 4. The red line is the same data binned in intervals of width 0.01 in orbital phase (≈46.7 minutes).
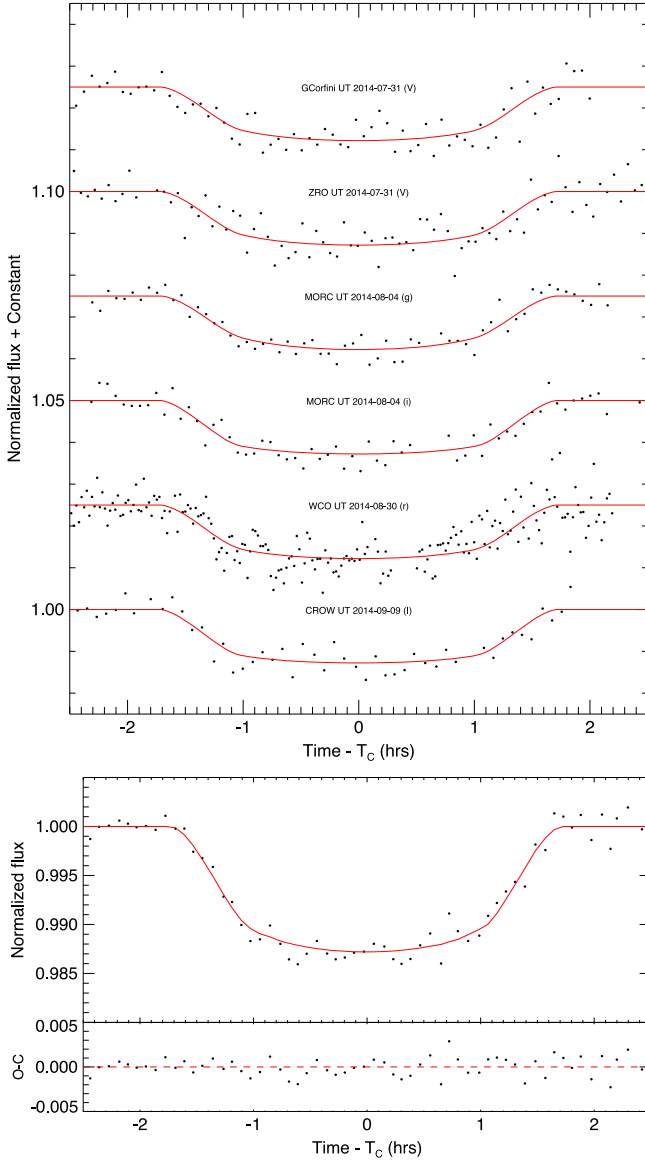

Figure 2. Top: follow-up photometry of KELT-8b primary transits. The source, date, and filter for each transit is annotated. The best-fit models are shown in red. Bottom: all follow-up transit light curves combined and binned in 5 minute intervals. This light curve is not used in the analysis and is shown simply to demonstrate the combined photometric precision of the follow-up light curves.

Table 1
Summary of Photometric Observations

| Telescope | UT | # | Filter | Cycle[a] | rms[b] | PNR[c] | α[d] |
	(2014)	Obs	Band	(s)	(10^{-3})	$\left(\frac{10^{-3}}{minutes}\right)$	
GCorfini	7-31	73	V	243	3.0	6.0	1.1
ZRO	7-31	110	V	216	3.5	6.6	1.9
MORC	8-04	65	g'	127	2.1	3.0	2.2
MORC	8-04	62	i'	127	2.3	3.3	2.6
WCO	8-30	209	r'	81	3.8	4.4	3.1
CROW	9-09	49	I_C	332	2.3	5.4	1.3

Notes.
[a] Cycle time in seconds, calculated as the mean of exposure time plus dead time during periods of back-to-back exposures. The MORC g' and i' exposures were alternating, so cycle time is calculated for exposures in both filters combined.
[b] rms of residuals from the best-fit model in units of 10^{-3}.
[c] Photometric noise rate in units of 10^{-3} minute^{-1}, calculated as rms/$\sqrt{\Gamma}$, where rms is the scatter in the light curve residuals and Γ is the mean number of cycles (exposure time and dead time) per minute during periods of back-to-back exposures (adapted from Fulton et al. 2011).
[d] Scaling factor applied to the uncertainties to ensure that the best-fitting model has $\chi_\nu^2 = 1$ (see Section 5).

Newtonian telescope and a SBIG STT-6303 ME CCD 1536 × 1024 pixel camera, giving a 59′ × 39′ field of view. No defocusing was applied, but the target and neighbor star were severely blended on the detector due to seeing. A photometric aperture was chosen that included both KELT-8 and its neighbor. The resulting light curve was corrected for blending, as described in Section 5.

2.2.3. Roberto Zambelli's Personal Observatory (ZRO)

We observed one full transit in the V_C filter on UT 2014-07-31 at ZRO. The telescope was not defocused and both stars were cleanly resolved from each other. The observations were obtained using a Meade LX 200 ACF GPS 12″ telescope, a $f/6.3$ focal reducer, and an SBIG ST8 XME 1530 × 1020 CCD with a pixel scale of 0.92 arcsec pixel^{-1} and a 23′ × 15′ field of view.

2.2.4. Westminster College Observatory (WCO)

We observed a full transit in the r' band at WCO in Pennsylvania on UT 2014-08-30. The observations were obtained using a Celestron 0.35 m C14 telescope with an

Table 2
Radial Velocities of KELT-8

BJD$_{TDB}$ (−2440000)	RV (m s^{-1})	σ_{RV} (m s^{-1})	BS (m s^{-1})	σ_{BS} (m s^{-1})
16884.7240398	−52.700	13.698	18.194	14.832
16886.7223760	16.089	11.487	60.348	22.517
16888.6894588	54.770	11.598	21.460	21.508
16890.6920118	−85.923	11.536	104.118	56.715
16891.6849308	39.139	11.894	−18.528	26.524
16892.6862628	120.081	10.732	15.611	12.552
16894.6776168	−30.453	11.729	−18.657	35.822
16895.6940738	98.475	11.258	18.095	18.990
16900.7203146	−99.117	11.290	−3.809	25.208
16903.7467735	−104.461	12.930	67.604	41.392
16905.6816215	91.985	13.023	6.130	15.736
16906.7226164	−90.377	12.995	117.227	77.109
16970.6342444	55.520	20.228	73.214	34.466

SBIG STL-6303E 3072 × 2048 CCD, giving a 24′ × 16′ field of view and 0.5 arcsec pixel^{-1}. The data were collected with the telescope in focus and the two stars were resolved from each other.

2.2.5. Canela's Robotic Observatory (CROW)

We observed one full transit in the I_C band at CROW in Portugal on UT 2014-09-09. The observations were obtained using a 0.3 m LX200 telescope with an SBIG ST-8XME 1530 × 1020 CCD, giving a 28′ × 19′ field of view and 1.11 arcsec pixel^{-1}. No telescope defocus was applied, but KELT-8 and the neighbor were blended on the detector due to seeing. A photometric aperture was selected to encircle the flux from both stars. The resulting light curve was corrected for blending, as described in Section 5.

2.3. High-resolution Spectroscopy

We collected a total of 13 RV measurements of KELT-8 using the Levy high-resolution optical spectrograph mounted at the Nasmyth foci of the Automated Planet Finder Telescope (APF) at Lick observatory (Burt et al. 2014; Radovan et al. 2014; Vogt et al. 2014). The measurements were collected between UT 2014 August 15 and UT 2014 November 9 and are presented in Table 2. We observed this star using the 2″ × 8″ slit for a spectral resolution of $R \approx 80,000$. We pass the starlight through a cell of gaseous iodine, which serves as a simultaneous wavelength and point-spread function (PSF) reference (Marcy & Butler 1992). Relative radial velocities are calculated by tracing the Doppler shift of the stellar spectrum with respect to the dense forest of iodine lines using a forward modeling technique described in Butler et al. (1996). Traditionally, a high signal-to-noise iodine-free observation of the same star is deconvolved with the instrumental PSF and used as the stellar template in the forward modeling process. However, in this case the star is too faint to collect the signal-to-noise needed for reliable deconvolution in a reasonable amount of time on the APF. Instead, we simulate this observation by using the SpecMatch software (E. A. Petigura et al. 2015, in preparation) to construct a synthetic template from the Coelho (2014) models and best-fit stellar parameters. This process is described in more detail in Section 4.
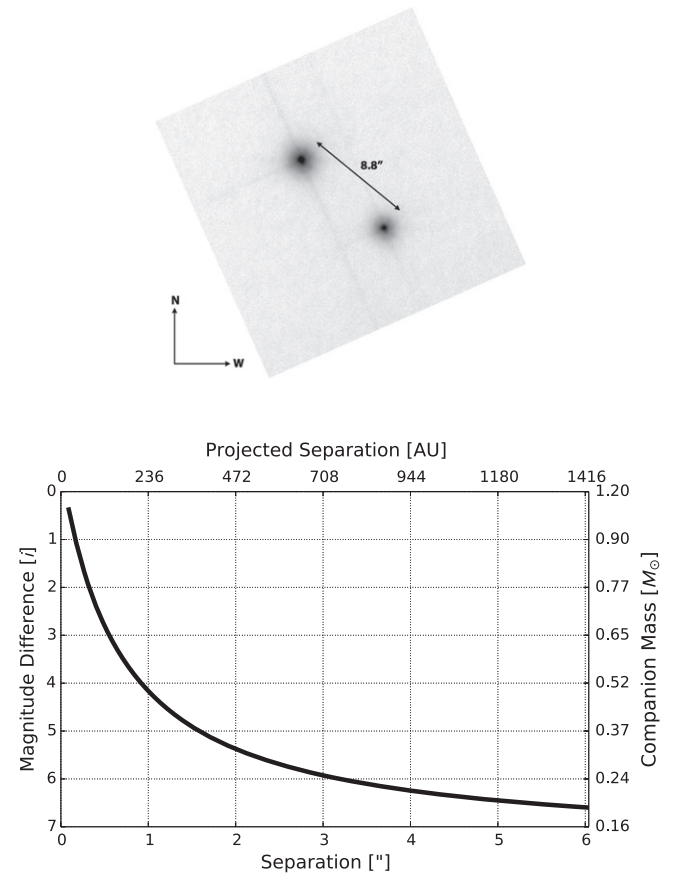

Figure 3. Top: Robo-AO image of KELT-8 showing the background giant star 8″.8 to the SW of KELT-8. Bottom: five σ contrast limit near KELT-8 derived from the Robo-AO image.

2.4. Adaptive Optics Imaging

We acquired visible-light adaptive optics images of KELT-8 using the Robo-AO system (Baranec et al. 2013, 2014) on the 60 inch Telescope at Palomar Observatory. On UT 2015 March 8, we observed KELT-8 in the Sloan-i' filter as a sequence of full-frame-transfer detector readouts at the maximum rate of 8.6 Hz for a total of 120 s of integration time. The individual images are corrected for detector bias and flat-fielding effects before being combined using post-facto shift-and-add processing, with KELT-8 as the tip-tilt star with 100% frame selection to synthesize a long-exposure image (Law et al. 2014).

We calculate the 5σ contrast limit as a function of angular separation by first determining the background noise level for concentric rings of width equal to the FWHM moving outward from the primary star. A simulated companion (a dimmed cutout of the primary star) is inserted into the closest ring with a random PA. An auto-companion detection code then searches for the simulated companion. If it is found, the companion is dimmed further and reinserted. This is continued until the companion is not found with a confidence greater than 5σ. We repeat this process for each annulus, and fit the sparse measurements with a function of the form $a - b/(r - c)$, where a, b, and c are free parameters in the fit and r is the radius from the target star. We convert contrast limits to mass limits

4

using the models of Baraffe et al. (2002). The resulting contrast and mass limits are presented in Figure 3.

3. STELLAR PROPERTIES

3.1. Keck/HIRES Spectroscopy

In order to obtain precise values for the stellar parameters, we collected a moderate signal-to-noise iodine-free observation using the HIRES spectrograph on the Keck I telescope (Vogt et al. 1994). We measured the effective temperature (T_{eff}), surface gravity (log g), iron abundance ([Fe/H]), and rotational velocity of the star ($v \sin i$) using the tools available in the SpecMatch software package (Petigura et al. 2015, in preparation). We first correct the observed wavelengths to be in the observer's rest frame by cross-correlating a solar model with the observed spectrum. Then we fit for T_{eff}, log g, [Fe/H], $v \sin i$, and the instrumental PSF using the underlying differential-evolution Markov Chain Monte Carlo (DE-MCMC; Ter Braak 2006) machinery of ExoPy (Fulton et al. 2013). At each point in the MCMC chains, a synthetic spectrum is created by interpolating the Coelho (2014) grid of stellar models for a set of T_{eff}, log g, and [Fe/H] values and solar alpha abundance. We convolve this synthetic spectrum with a rotational plus mactroturbulance broadening kernel using the prescriptions of Valenti & Fischer (2005) and Hirano et al. (2011). Finally, we perform another convolution with a Gaussian kernel to account for the instrumental PSF, and the synthetic spectrum is compared with the observed spectrum using χ^2 to assess the goodness of fit. The priors are uniform in T_{eff}, log g, and [Fe/H], but we assign a Gaussian prior to the instrumental PSF that encompasses the typical variability in the PSF width caused by seeing changes and guiding errors. Five echelle orders of the spectrum are fit separately and the resulting posterior distributions are combined before taking the median values for each parameter.

Parameter uncertainties are estimated as the scatter in spectroscopic parameters given by SpecMatch relative to the values in Valenti & Fischer (2005) for 352 of the stars in their sample and 76 stars in the Huber et al. (2012) asteroseismic sample. Systematic trends in SpecMatch values as a function of T_{eff}, log g, and [Fe/H] relative to these benchmark samples are fit for and removed in the final quoted parameter values. More details about the benchmark comparison and calibrations will be available in E. A. Petigura et al. (2015, in preparation). These spectroscopic parameters are then used as input priors for the global fit discussed in Section 5. The best-fit spectroscopically determined stellar parameters are log g = 4.23 ± 0.08, [Fe/H] = 0.272 ± 0.038, and T_{eff} = 5754^{+54}_{-55} K.

The log g derived from spectroscopy is only marginally consistent with the log g derived from the global fit ($4.078^{+0.049}_{-0.054}$). The log g value measured from the transit light curves is likely more reliable because log g can be a difficult quantity to measure from high-resolution spectroscopy alone. We perform a global analysis both with and without the spectroscopic log g as a prior (see Section 5).

We also collected a single exposure with the iodine cell in the light path with a slightly higher signal-to-noise ratio (S/N) to establish a long-term baseline for possible follow-up of this target with Keck in the future. We used this observation to extract the log R'_{HK} stellar activity metric. We find that
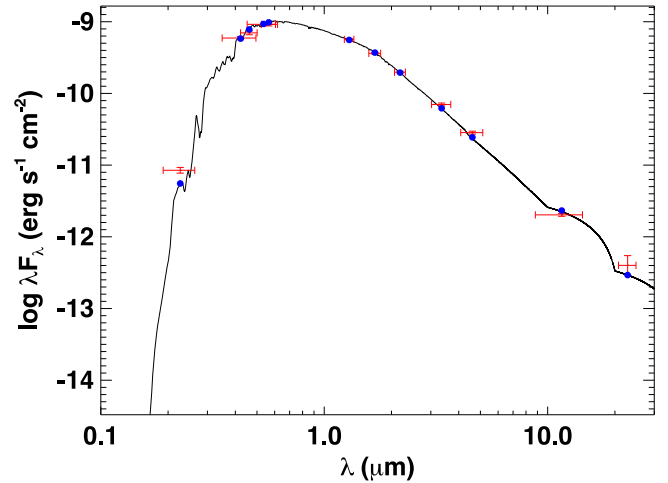

Figure 4. SED fit to KELT-8. The red crosses are the photometry measurements. The vertical errors are the 1σ photometric uncertainties, and the horizontal error bars are the effective widths of the passbands. The leftmost point (*GALEX* NUV) was omitted from the fit due to possible contamination from the neighboring star at 8″.8 separation. The black line is the best-fit stellar atmosphere model and the blue points are the predicted passband-integrated fluxes of the model corresponding to our observed photometric bands.

log R'_{HK} = −5.108, which indicates that the star is very chromospherically quiet.

3.2. Spectral Energy Distribution (SED)

We estimate the distance and reddening to KELT-8 by fitting the B-band through the *WISE* W4-band SED to the Kurucz (1979) stellar atmosphere models. We also found a *GALEX* NUV measurement in the literature (Bianchi et al. 2011), however this measurement shows a large excess in flux relative to the SED compatible with all other measurements. Because the PSF of *GALEX* in the NUV band is 4″.9, we suspect the *GALEX* measurement is contaminated by the visual companion 8″.8 away, and omit this measurement from the fit. The *WISE* measurements also have a large PSF relative to the separation between the two components, but we do not find any evidence for significant contamination. We fix T_{eff}, log g, and [Fe/H] to the best-fit values in Table 4 and leave distance (d) and reddening (A_V) as free parameters. We find best-fit parameters of A_V = 0.15 ± 0.06 magnitudes and d = 236 ± 9 pc with a reduced χ^2 = 3.7 (considering only the flux uncertainty and not the uncertainty in the model). This agrees quite well with the distance of 233 pc estimated by Pickles & Depagne (2010).

3.3. Evolutionary State

We estimate the age of KELT-8 by fitting Yonsei-Yale isochrones to the values of T_{eff}, log g, and [Fe/H] given in Table 4. We fix the stellar mass to the value of $M_* = 1.211 \, M_\odot$ listed in Table 4. Our best-fit stellar parameters indicate that the star happens to fall on a very rapid part of the evolutionary track, the so-called "blue hook" just prior to crossing the Hertzsprung gap (see Figure 5). In principle, this would allow for a very precise measurement of the stellar age, however, the measurement errors on T_{eff} and log g do not allow us to locate the star's exact position within the blue hook. We conservatively quote an age range of 4.9–5.8 Gyr that spans the entire blue hook. Note that the uncertainty on the age likely does not follow a Gaussian distribution because the rapid evolution through the blue hook
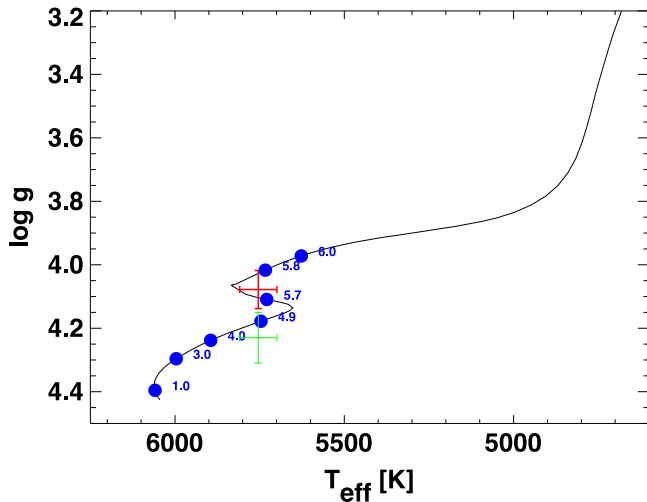
Figure 5. Yonsei-Yale isochrone fit for KELT-8. The solid black line is the isochrone for a star with the mass and metallically of KELT-8 listed in Table 4. The red cross is the position of KELT-8, and the blue points label various ages along the evolutionary track. The green cross is the position of KELT-8 using the spectroscopically determined $\log g$. The "blue hook" is the kink in the track where the star's $T_{\rm eff}$ increases while $\log g$ decreases for a short amount of time between an age of 4.9 and 5.8 Gyr.

means that stars on the blue hook should be rare. It is much more likely that it falls on one side or the other of the blue hook simply because stars spend such a small fraction of the lifetimes on the blue hook. A more detailed evolutionary analysis that includes rotation, chemical composition, and a full consideration of all relevant priors is needed to determine the exact evolutionary state of KELT-8.

3.4. Unrelated Visual Companion

KELT-8 was identified as a visual binary in 1905 by French astronomer Abel Pourteau (Pourteau 1933). Figure 3 shows KELT-8 and the fainter visual companion 8″8 to the SW clearly resolved. In addition to the discovery astrometry, further astrometric measurements were made in 1951 (Gellera 1984, 1990), 2000 (Cutri et al. 2003), and 2001 (Hartkopf et al. 2013b). These measurements all show a trend of decreasing separation and increasing position angle, although the scatter in the pre-CCD measurements is large (see Figure 6). We also measured astrometry from our Robo-AO data and find that it is consistent with this trend, especially if only the CCD measurements are considered. This is consistent with KELT-8 moving with the constant proper motions given in Table 3 and the companion being stationary in the background.

We also collected an APF spectrum of the secondary component and used the SpecMatch pipeline to extract stellar parameters. We cross-correlated the best-fitting model with the observed spectrum after correcting for the Earth's barycentric motion to determine an absolute systemic velocity. SpecMatch returned $T_{\rm eff} = 4702 \pm 60$, $\log g = 2.77 \pm 0.08$, and $[{\rm Fe/H}] = 0.01 \pm 0.04$, which is consistent with the companion being a G or K giant with an intrinsic luminosity much greater than that of KELT-8. Because this component appears approximately one magnitude fainter than KELT-8 in the V band, it must be in the background. In addition, the systemic RV of the secondary of $34 \pm 1\,{\rm km\,s^{-1}}$ is highly discrepant with the velocity of KELT-8 $(-31.2 \pm 0.3\,{\rm km\,s^{-1}})$. These lines
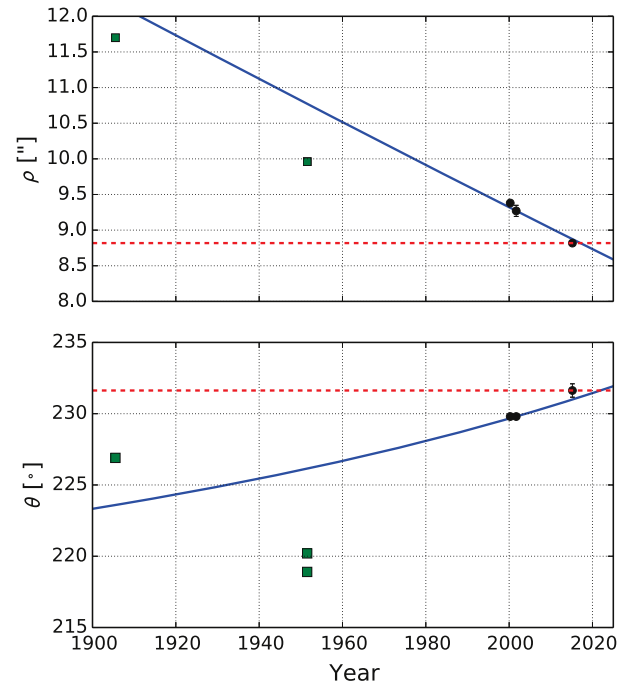

Figure 6. Astrometry measurements of KELT-8. The green squares were measured using astrometric eyepieces or photographic plates. The black points were measured using CCD data and the most recent point is from our Robo-AO observation. The blue lines are the predicted change in separation (upper panel) and position angle (lower panel), assuming that the star 8″8 to the SW of KELT-8 is in the background with negligible proper motion and KELT-8 has a constant proper motion with the values given in Table 3. The dashed black line is a model assuming that the two components are physically bound and the orbital motion of the pair is negligible during the span of observations.

of evidence all suggest that the two stars are physically unrelated.

3.5. UVW Space Motion

We evaluate the motion of KELT-8 through the galaxy. The absolute RV measured from the APF spectra of KELT-8 is $-31.2 \pm 0.3\,{\rm km\,s^{-1}}$, and the proper motions from Tycho-2 are -13.7 ± 1.4 and $-29.5 \pm 1.3\,{\rm mas\,yr^{-1}}$ in R.A. and decl., respectively. These values transform to U,V,W space motions of 20.6 ± 1.7, -32.6 ± 1.2, and $0.7 \pm 1.5\,{\rm km\,s^{-1}}$, respectively, making KELT-8 an unambiguous member of the thin disk stellar population (Bensby et al. 2003). Because it is not a halo star, this further supports our adoption of the stellar $\log g$ derived from the transit fit, which gives stellar parameters (particularly metallicity) that are much more common for thin disk stars (Ivezić et al. 2012).

4. SYNTHETIC TEMPLATE RADIAL VELOCITIES

Iodine-based radial velocities are traditionally derived using a forward modeling process that requires three primary ingredients: a template spectrum of the star with the iodine out of the light path, an ultra-high-resolution spectrum of the iodine absorption for the particular cell in use, and a description of the instrumental PSF (Butler et al. 1996). The stellar template and the iodine spectrum are multiplied together then convolved with the PSF to match the observed spectrum taken through iodine. The stellar template is usually an observation of the same star taken at 2–3 times higher S/N than the iodine observations and using a narrower slit for higher resolution.

Table 3
Adopted Stellar Properties of KELT-8

Parameter (Units)	Value	Source	Reference
Names	HD 343246	SIMBAD	⋯
	GSC 02109-00049	SIMBAD	⋯
	2MASS J18531332 +2407385	SIMBAD	⋯
	TYC 2109-49-1	SIMBAD	⋯
	WDS 18533+2407	WDS	Hartkopf et al. (2013a)
Spectral type	G2V	this work	⋯
R.A. (J2000)	18 53 13.3216	Tycho-2	Høg et al. (2000)
Decl. (J2000)	+24 07 38.603	Tycho-2	Høg et al. (2000)
U^a (km s^{-1})	20.6 ± 1.7	this work	⋯
V (km s^{-1})	-32.6 ± 1.2	this work	⋯
W (km s^{-1})	0.7 ± 1.5	this work	⋯
R.A. proper motion (mas yr^{-1})	-13.7 ± 1.4	Tycho-2	Høg et al. (2000)
Decl. proper motion (mas yr^{-1})	-29.5 ± 1.3	Tycho-2	Høg et al. (2000)
Systemic velocity (km s^{-1})	-31.2 ± 0.3	this work	⋯
NUV (mag)	16.884 ± 0.1^b	*GALEX*	Bianchi et al. (2011)
B_T (mag)	11.713 ± 0.057	Tycho-2	Høg et al. (2000)
V_T (mag)	10.925 ± 0.048	Tycho-2	Høg et al. (2000)
B (mag)	11.545 ± 0.065	ASCC	Kharchenko (2001)
V (mag)	10.833 ± 0.054	ASCC	Kharchenko (2001)
J (mag)	9.586 ± 0.026	2MASS	Cutri et al. (2003)
H (mag)	9.269 ± 0.032	2MASS	Cutri et al. (2003)
K (mag)	9.177 ± 0.021	2MASS	Cutri et al. (2003)
W1 (mag)	11.664 ± 0.05	*WISE*	Cutri et al. (2014)
W2 (mag)	12.302 ± 0.05	*WISE*	Cutri et al. (2014)
W3 (mag)	14.17 ± 0.05	*WISE*	Cutri et al. (2014)
W4 (mag)	15.193 ± 0.339	*WISE*	Cutri et al. (2014)
$v \sin i$ (km s^{-1})	3.7 ± 1.5	this work	⋯
Age (Gyr)	$5.4^{+0.4}_{-0.5}$	this work	⋯
Distance (pc)	236 ± 9	this work	⋯
A_V	0.15 ± 0.06	this work	⋯
$\log R'_{HK}$	-5.108	this work	⋯

Notes.
[a] Positive U is in the direction of the Galactic Center.
[b] Likely contaminated by the neighbor star 8″.8 away.

Because the PSF is constantly changing on a slit-fed spectrograph due to changes in the slit illumination caused by variable seeing and guiding patterns, we need to deconvolve this stellar template to remove distortions in the line profile. This deconvolution process also requires a measurement of the instrumental PSF. By construction, we do not have a simultaneous PSF calibration for the template observations as we do for the iodine observations. We instead rely on bracketing observations of rapidly rotating B stars through iodine, but the PSF is never exactly the same for any two observations, and this non-simultaneous calibration introduces errors. In addition, the deconvolution process is inherently unstable because we are essentially trying to create a view of the star at infinite spectral resolution using data taken at finite spectral resolution. Collecting as much signal as possible for the template observation helps ensure that this component of the model is not the limiting factor on the final RV precision.
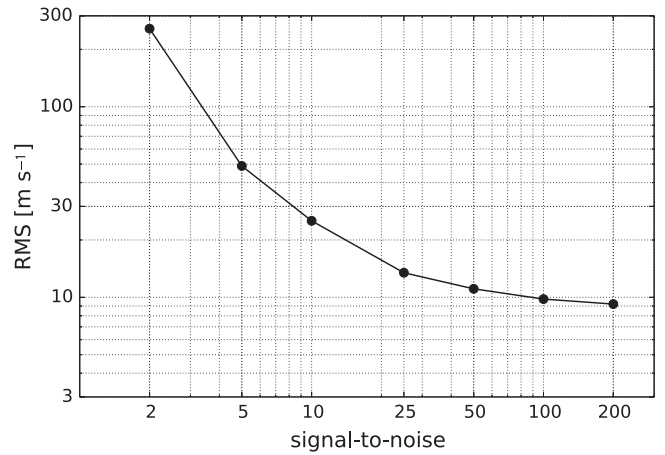

Figure 7. Synthetic template RV performance as a function of S/N of the iodine observations. Artificial Gaussian noise was injected into the spectra of a well-known RV standard star (HD 9407) before running them through the RV extraction pipeline for all data points, excluding the one at S/N = 200. The synthetic template technique shows predictable and consistent performance down to extremely low S/N s and a model-limited noise floor of $\approx$10 m s^{-1}.

For faint stars ($V > 12$), iodine exposures on Keck/HIRES can take 45–60 min each. Collecting a template at 2–3 times higher S/N would take a significant fraction of a night. At APF, the situation is even worse due to its much smaller aperture (2.4 m versus 10 m). When collecting reconnaissance RVs for a new candidate from a transit survey to look for various false positive scenarios only 2–3 RVs may be needed before a false alarm scenario can be confirmed or eliminated. Collecting a high S/N template can take as much time as the entire set of RV observations, effectively doubling the observational time needed in these scenarios.

In order to circumvent these problems, we developed a technique that uses a synthetic template using the Coelho (2014) models and spectral synthesis code from SpecMatch. We first determine the spectral parameters from the best available information. Approximate values for T_{eff}, log g, and [Fe/H] can be obtained using spectral regions outside the iodine absorption regime, photometry, or low-resolution spectroscopy. We normally use a single echelle order redward of the iodine regime to estimate $v \sin i$. T_{eff} and $v \sin i$ have the most drastic impact on the resulting RV, but fortunately T_{eff} is the easiest parameter to estimate in the absence of a high-resolution spectrum and $v \sin i$ can be estimated with very few spectral lines. Once the spectral parameters are established, we synthesize the full spectrum within the iodine region setting the instrumental PSF width to zero. This provides an extremely high-resolution, noise-free stellar template to use as one of the inputs to the normal RV extraction code. This foregoes the need for deconvolution and saves valuable telescope time.

This technique is not perfect due to inaccuracies in the model spectra. Spectral lines are missing in some regions, blended lines may only be accounted for as a single line, and the central wavelengths of lines may be slightly inaccurate. This means that when using these synthetic templates we can never achieve the 2–3 m s^{-1} precision that we can obtain using the traditional technique for bright stars. Figure 7 shows a velocity rms for the RV standard star (HD 9407) as a function of S/N of the iodine observations using the synthetic template technique. We artificially inject Gaussian noise into the spectra before sending them through the normal RV extraction pipeline. We use an
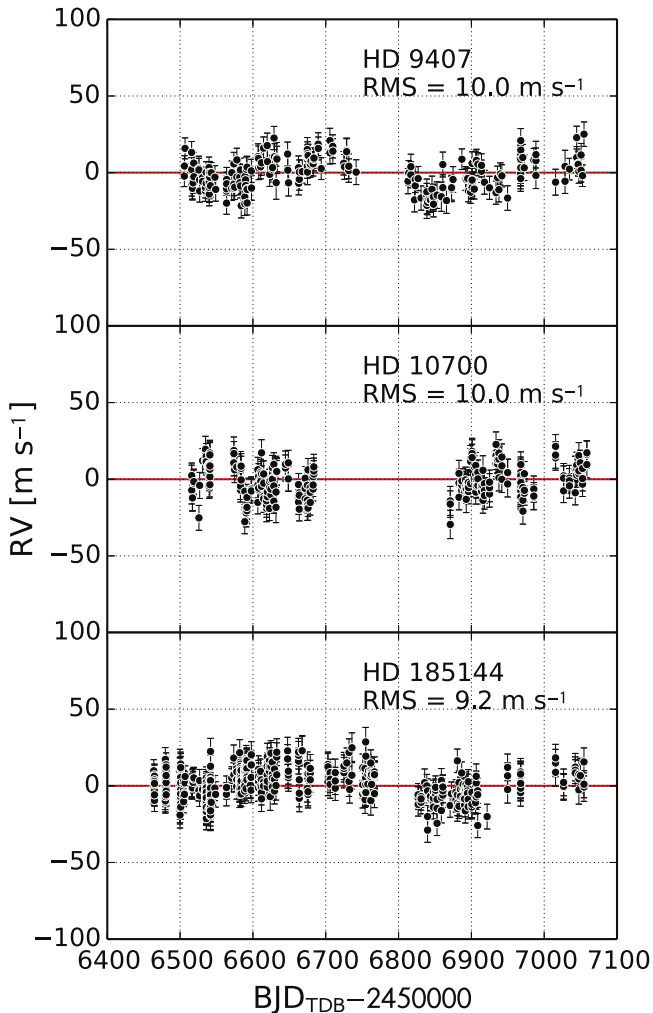
Figure 8. Synthetic template RV performance for three RV standard stars. Artificial Gaussian noise was injected into all spectra for each star, so that S/N = 50 for each spectrum. This is approximately the same S/N that was collected for each KELT-8 observation. The RV rms is about 10 m s^{-1} for each star.

exposure meter to expose to S/N = 200 for all normal observations, and the highest S/N datapoint shown in Figure 7 has no artificial noise injected. The RV rms monotonically decreases down to extremely low S/N levels with a noise floor at just below 10 m s^{-1} for high S/N. Two other RV standard stars were also run through the synthetic template pipeline with S/N artificially decreased to match that of our KELT-8 observations. In each case, the synthetic template RV rms was about 10 m s^{-1} (see Figure 8). We use this technique to extract the RVs from the APF data for KELT-8 and achieve a median per-measurement precision of 11.8 m s^{-1}.

While our technique is unique for iodine-based RVs in the optical, several other very similar techniques have been developed to extract high-precision RVs. Bailey et al. (2012) and Tanner et al. (2012) use interpolated model atmospheres for their templates, but instead of an iodine cell they use telluric lines for their PSF and wavelength calibration. They were able to achieve ~50 m s^{-1} precision in the near-infrared with NIRSPEC on Keck. Other telluric-calibrated techniques have proven successful in the optical with HIRES to obtain

velocities to 100 m s^{-1} precision (Chubak et al. 2012). Johnson et al. (2006) perturb an existing empirical template of a similar star in order to avoid the need to collect a unique template for each star observed. They were able to achieve a prescision of 3–5 m s^{-1} using these perturbed empirical templates.

5. PLANETARY CHARACTERIZATION

5.1. Global Fit

We determine the system's orbital and planetary properties by performing a global analysis on the RVs, spectroscopic stellar parameters, and follow-up light curves using a custom version of EXOFAST (Eastman et al. 2013). Our global analysis technique is very similar to that used for the previous KELT discoveries (Beatty et al. 2012; Siverd et al. 2012; Pepper et al. 2013; Collins et al. 2014; Bieryla et al. 2015). The EXOFAST package uses a DE-MCMC fitting routing to extract the median parameter values and 68% confidence intervals using all available data, and these values are presented in Table 4. Constraints on the stellar parameters M_* and R_* are also included using the Yonsei-Yale stellar models and spectroscopically derived values for T_{eff} and [Fe/H] as input priors. Before running the MCMC chains, a best-fit solution is found using an AMOEBA χ^2 minimization routine, and the photometric and RV uncertainties are scaled such that $\chi^2_\nu = 1$. The scaling factors for the photometric data are listed in Table 1 and the scaling factor applied to the APF RV uncertainties is 1.44. The scaled uncertainties include both instrumental and astrophysical noise sources, which ensures that the widths of the final posterior properly represent the uncertainties in the model parameters.

As described in Collins et al. (2014), we identify trend data sets that best improve the individual light curve fits using AIJ. These trend data sets are included as input to EXOFAST, along with the undetrended light curve data. As part of the global fit, EXOFAST simultaneously finds the best transit model fit and removes linear trends that are correlated with different combinations of air mass, time, FWHM, and CCD position.

The light from the visual companion to KELT-8 was included in the photometric aperture of the GCorfini and ZRO light curves. We corrected for this by measuring the flux ratio of the primary to secondary component in the well-resolved MORC data. The flux ratios are 1.24 and 1.44 in the g' and i' bands, respectively. We then interpolated/extrapolated these flux ratios to the central wavelengths of the V and Ic GCorfini and ZRO light curves, and corrected the input light curves for the dilution before fitting them in EXOFAST. We also ran the global fit excluding these two transits, and found that all parameters are consistent to well within 1σ. This gives us confidence that these blended light curves are not biasing the inferred parameters.

We ran four permutations of the global fit using slightly different input priors and constraints. First, we assert constraints on the stellar mass and radius from the Yonsei-Yale isochrones and a uniform prior on log g. We adopt the parameter values from this fit for all analysis and interpretation. Second, we performed the same fit using constraints from the Torres et al. (2010) relations instead. These two fits produced nearly identical results. Then we performed these same two global fits, but imposed a prior on log g from the high-resolution spectroscopy. The log g derived from spectroscopy is slightly higher and only marginally consistent with the log g

Table 4
Median Values and 68% Confidence Intervals for KELT-8b

Parameter	Units	Adopted Value (YY)	Value (Torres)	Value (YY + log g prior)	Value (Torres + log g prior)
Stellar Parameters					
M_*	Mass ($M_\odot$)	$1.211^{+0.078}_{-0.066}$	$1.233^{+0.066}_{-0.063}$	$1.188^{+0.067}_{-0.063}$	$1.211^{+0.060}_{-0.059}$
R_*	Radius ($R_\odot$)	$1.67^{+0.14}_{-0.12}$	$1.69^{+0.15}_{-0.12}$	$1.570^{+0.099}_{-0.097}$	1.577 ± 0.096
L_*	Luminosity ($L_\odot$)	$2.74^{+0.51}_{-0.40}$	$2.79^{+0.54}_{-0.41}$	$2.42^{+0.35}_{-0.32}$	$2.44^{+0.34}_{-0.31}$
ρ_*	Density (cgs)	$0.369^{+0.073}_{-0.067}$	$0.363^{+0.078}_{-0.072}$	$0.433^{+0.076}_{-0.061}$	$0.436^{+0.078}_{-0.062}$
$\log g_*$	Surface gravity (cgs)	$4.078^{+0.049}_{-0.054}$	$4.075^{+0.054}_{-0.061}$	$4.121^{+0.043}_{-0.041}$	$4.125^{+0.045}_{-0.042}$
$T_{\rm eff}$	Effective temperature (K)	5754^{+54}_{-55}	5749 ± 59	5748 ± 53	5750 ± 59
[Fe/H]	Metallicity	0.272 ± 0.038	0.270 ± 0.039	$0.270^{+0.038}_{-0.039}$	$0.271^{+0.040}_{-0.039}$
Planetary Parameters					
e	Eccentricity	$0.035^{+0.050}_{-0.025}$	$0.037^{+0.057}_{-0.027}$	$0.028^{+0.033}_{-0.019}$	$0.027^{+0.033}_{-0.020}$
ω_*	Argument of periastron (degrees)	85^{+87}_{-97}	85^{+82}_{-93}	-80^{+120}_{-130}	-80^{+120}_{-130}
a	Semi-major axis (AU)	$0.04571^{+0.00096}_{-0.00084}$	$0.04599^{+0.00081}_{-0.00079}$	$0.04542^{+0.00084}_{-0.00082}$	$0.04571^{+0.00074}_{-0.00075}$
M_P	Mass ($M_{\rm J}$)	$0.867^{+0.065}_{-0.061}$	$0.876^{+0.063}_{-0.061}$	$0.855^{+0.062}_{-0.061}$	$0.869^{+0.061}_{-0.060}$
R_P	Radius ($R_{\rm J}$)	$1.86^{+0.18}_{-0.16}$	$1.88^{+0.19}_{-0.16}$	1.73 ± 0.13	1.74 ± 0.13
ρ_P	Density (cgs)	$0.167^{+0.047}_{-0.038}$	$0.163^{+0.049}_{-0.039}$	$0.205^{+0.051}_{-0.039}$	$0.205^{+0.052}_{-0.040}$
$\log g_P$	Surface gravity	$2.793^{+0.072}_{-0.075}$	$2.786^{+0.076}_{-0.075}$	$2.850^{+0.065}_{-0.063}$	$2.853^{+0.066}_{-0.064}$
$T_{\rm eq}$	Equilibrium temperature (K)	1675^{+61}_{-55}	1679^{+66}_{-57}	1629^{+47}_{-48}	1628^{+46}_{-47}
Θ	Safronov number	$0.0351^{+0.0040}_{-0.0037}$	$0.0346^{+0.0041}_{-0.0038}$	$0.0378^{+0.0039}_{-0.0035}$	$0.0377^{+0.0039}_{-0.0035}$
$\langle F \rangle$	Incident flux (10^9 erg s^{-1} cm^{-2})	$1.78^{+0.27}_{-0.22}$	$1.80^{+0.29}_{-0.23}$	$1.60^{+0.19}_{-0.18}$	$1.59^{+0.19}_{-0.18}$
RV Parameters					
T_P	Time of periastron (BJD$_{\rm TDB}$-2450000)	$6870.47^{+0.75}_{-0.86}$	$6870.47^{+0.70}_{-0.83}$	$6869.0^{+1.1}_{-1.2}$	$6869.0^{+1.1}_{-1.2}$
K	RV semi-amplitude (m s^{-1})	104.0 ± 6.4	104.0 ± 6.4	104.1 ± 6.5	104.4 ± 6.5
M_P/M_*	Mass ratio	$0.000683^{+0.000045}_{-0.000044}$	$0.000679^{+0.000044}_{-0.000043}$	$0.000687^{+0.000045}_{-0.000044}$	0.000685 ± 0.000044
$\gamma_{\rm APF}$	m s^{-1}	6.1 ± 4.9	6.0 ± 5.0	6.7 ± 4.9	$6.7^{+4.9}_{-5.0}$
$e \cos \omega_*$	...	$0.001^{+0.024}_{-0.021}$	$0.001^{+0.025}_{-0.021}$	$0.001^{+0.022}_{-0.019}$	$0.001^{+0.022}_{-0.018}$
$e \sin \omega_*$	...	$0.012^{+0.063}_{-0.025}$	$0.014^{+0.071}_{-0.027}$	$-0.001^{+0.029}_{-0.032}$	$-0.001^{+0.028}_{-0.034}$
Primary Transit Parameters					
R_P/R_*	Planet to star radius ratio	0.1145 ± 0.0026	0.1146 ± 0.0026	0.1133 ± 0.0025	0.1132 ± 0.0025
a/R_*	Semi-major axis in stellar radii	$5.90^{+0.37}_{-0.38}$	$5.87^{+0.39}_{-0.42}$	$6.22^{+0.34}_{-0.31}$	$6.23^{+0.35}_{-0.31}$
i'	Inclination (degrees)	$82.65^{+0.81}_{-1.0}$	$82.56^{+0.88}_{-1.2}$	83.36 ± 0.69	$83.38^{+0.69}_{-0.70}$
b	Impact parameter	$0.741^{+0.027}_{-0.033}$	$0.743^{+0.027}_{-0.033}$	$0.722^{+0.028}_{-0.036}$	$0.722^{+0.029}_{-0.037}$
δ	Transit depth	0.01311 ± 0.00059	$0.01313^{+0.00061}_{-0.00059}$	$0.01283^{+0.00058}_{-0.00057}$	0.01282 ± 0.00057
τ	Ingress/egress duration (days)	$0.0303^{+0.0038}_{-0.0035}$	$0.0305^{+0.0039}_{-0.0036}$	$0.0280^{+0.0033}_{-0.0032}$	$0.0280^{+0.0034}_{-0.0032}$
T_{14}	Total duration (days)	$0.1444^{+0.0034}_{-0.0033}$	0.1446 ± 0.0034	$0.1423^{+0.0032}_{-0.0031}$	0.1423 ± 0.0032
u_{1I}	Linear Limb-darkening	$0.2961^{+0.0092}_{-0.0088}$	$0.2966^{+0.0096}_{-0.0093}$	$0.2977^{+0.0089}_{-0.0087}$	$0.2975^{+0.0096}_{-0.0092}$
u_{2I}	Quadratic Limb-darkening	$0.2793^{+0.0044}_{-0.0049}$	$0.2790^{+0.0047}_{-0.0052}$	$0.2782^{+0.0042}_{-0.0047}$	$0.2783^{+0.0046}_{-0.0051}$
$u_{1{\rm Sloang'}}$	Linear Limb-darkening	0.607 ± 0.015	$0.607^{+0.016}_{-0.015}$	0.608 ± 0.015	$0.608^{+0.016}_{-0.015}$
$u_{1{\rm Sloang'}}$	Quadratic Limb-darkening	$0.184^{+0.010}_{-0.011}$	$0.184^{+0.011}_{-0.012}$	$0.183^{+0.010}_{-0.011}$	$0.184^{+0.011}_{-0.012}$
$u_{1{\rm Sloang'}}$	Linear Limb-darkening	$0.3178^{+0.0097}_{-0.0092}$	$0.3183^{+0.010}_{-0.0097}$	$0.3193^{+0.0094}_{-0.0091}$	$0.3192^{+0.010}_{-0.0096}$
$u_{1{\rm Sloang'}}$	Quadratic Limb-darkening	$0.2789^{+0.0046}_{-0.0052}$	$0.2786^{+0.0050}_{-0.0056}$	$0.2779^{+0.0045}_{-0.0051}$	$0.2779^{+0.0049}_{-0.0055}$
$u_{1{\rm Sloang'}}$	Linear Limb-darkening	$0.410^{+0.012}_{-0.011}$	0.410 ± 0.012	$0.411^{+0.012}_{-0.011}$	0.411 ± 0.012
$u_{1{\rm Sloang'}}$	Quadratic Limb-darkening	$0.2725^{+0.0062}_{-0.0070}$	$0.2722^{+0.0066}_{-0.0074}$	$0.2715^{+0.0066}_{-0.0068}$	$0.2717^{+0.0066}_{-0.0074}$
u_{1V}	Linear Limb-darkening	$0.487^{+0.013}_{-0.012}$	$0.488^{+0.014}_{-0.013}$	$0.488^{+0.013}_{-0.012}$	$0.488^{+0.014}_{-0.013}$
u_{2V}	Quadratic Limb-darkening	$0.2446^{+0.0077}_{-0.0088}$	$0.2442^{+0.0082}_{-0.0093}$	$0.2435^{+0.0078}_{-0.0087}$	$0.2437^{+0.0082}_{-0.0093}$
Linear Ephemeris from Follow-up Transits					
P	Period (days)	3.24406 ± 0.00016	3.24406 ± 0.00016	3.24406 ± 0.00016	3.24406 ± 0.00016
T_0	Time of transit (BJD$_{\rm TDB}$-2450000)	6883.4803 ± 0.0007	6883.4803 ± 0.0007	6883.4804 ± 0.0007	6883.4804 ± 0.0007
Predicted Secondary Eclipse Parameters					
T_S	Time of eclipse (BJD$_{\rm TDB}$-2450000)	$6868.886^{+0.049}_{-0.043}$	$6868.887^{+0.050}_{-0.044}$	$6868.886^{+0.044}_{-0.039}$	$6872.130^{+0.044}_{-0.038}$
b_S	Impact parameter	$0.763^{+0.097}_{-0.057}$	$0.769^{+0.11}_{-0.061}$	$0.718^{+0.051}_{-0.054}$	$0.716^{+0.051}_{-0.055}$
τ_S	Ingress/egress duration (days)	$0.0327^{+0.016}_{-0.0059}$	$0.0332^{+0.019}_{-0.0065}$	$0.0277^{+0.0054}_{-0.0042}$	$0.0276^{+0.0053}_{-0.0042}$
$T_{S,14}$	Total duration (days)	$0.1436^{+0.0034}_{-0.0049}$	$0.1435^{+0.0036}_{-0.0060}$	$0.1419^{+0.0033}_{-0.0041}$	$0.1418^{+0.0034}_{-0.0042}$

derived from transits. The results from all four fits are presented in Table 4. The differences in parameter values from these four fits give an estimate of our systematic uncertainty, which appears to be similar to the statistical uncertainties for most parameters. This gives us confidence that our parameter uncertainties are properly estimated and that our interpretations of physical parameters (such as the large planetary radius) are robust.
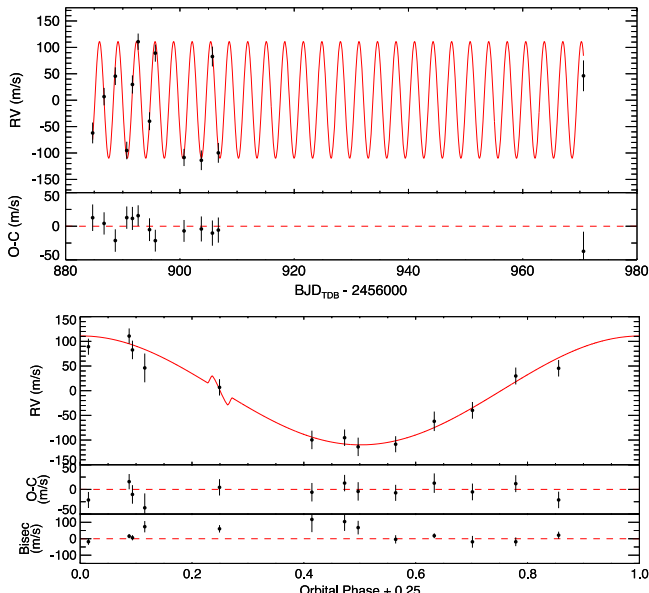
Figure 9. Top: APF RVs and residuals for KELT-8. The best-fit model is shown in red. Bottom: RVs and bisector span measurements phase-folded to the best-fit linear ephemeris. The best-fit model is shown in red. The predicted Rossiter–McLaughlin effect assumes perfect spin–orbit alignment and it is not constrained by our data.

We measure an eccentricity for KELT-8b of $e = 0.035^{+0.050}_{-0.025}$, which deviates from zero by only 1.4σ. The measurement of eccentricity is easily biased to artificially larger values and a significance of $\geqslant 2.5\sigma$ is generally accepted as being required to claim a non-circular orbit (Lucy & Sweeney 1971). Although we do not find any significant eccentricity in the system, moderate eccentricity is not unprecedented in other hot Jupiters (e.g., HAT-P-2b, XO-3b, WASP14b, HAT-P-31b; Bakos et al. 2007; Joshi et al. 2009; Winn et al. 2009; Kipping et al. 2011). We allow for eccentricity to vary as a free parameter in order to ensure that the errors on all other parameters are not underestimated.

We searched for possible transit timing variations (TTVs) in the system by allowing the transit times for each of the follow-up light curves to vary. The ephemeris is constrained by the RV data and a prior imposed from the KELT discovery data. We find no evidence for significant TTVs. The individual transit times are presented in Table 5 and Figure 10.

After the completion of the global fit we then derive a linear ephemeris. The period is constrained by the RV data and comes from the global fit. We fit for T_0 using the transit times from the follow-up light curves. The best-fit linear ephemeris is listed in Table 4. We find $P = 3.24406 \pm 0.00016$ days and $T_0 = 2456883.4803 \pm 0.0007$ BJD$_{\mathrm{TDB}}$. The χ^2 for the linear ephemeris fit is 7.4 with 4° of freedom, which indicates that a linear ephemeris adequately describes the observed transit times.

5.2. False-positive Assessment

We calculate bisector spans (BS) for each of the APF spectra in order to investigate possible blend scenarios in which the measured RV variations are caused by line distortions that arise from an unresolved eclipsing binary instead of the true reflex motion of the star. In the case that the measured Doppler shifts are caused by a second set of incompletely resolved stellar lines from a luminous companion, we would expect to see BSs that

Table 5
Transit Times for KELT-8b

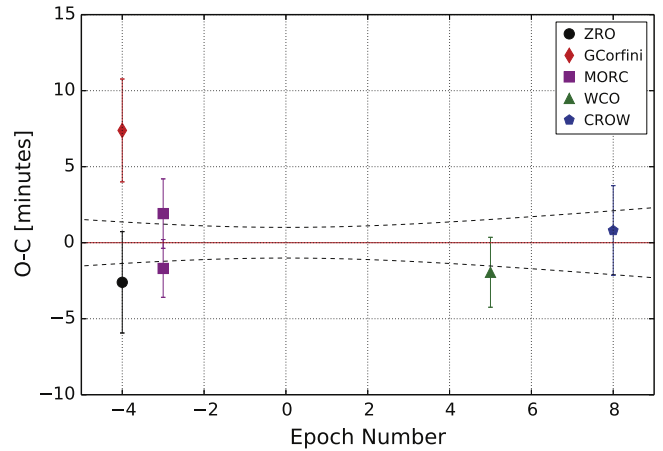| Epoch	T_C (BJD$_{\mathrm{TDB}}$)	σ_{T_C} (s)	O–C (s)	O–C (σ_{T_C})	Telescope
−4	2456870.502251	200	−156.3	−0.78	ZRO
−4	2456870.509188	203	443.1	2.18	GCorfini
−3	2456873.746945	114	−101.5	−0.89	MORC
−3	2456873.749450	137	114.9	0.83	MORC
5	2456899.699249	138	−116.7	−0.85	WCO
8	2456909.433338	177	48.2	0.27	CROW

Figure 10. Residuals of the transit times from the best-fit ephemeris for the follow-up light curves. The source of each transit time is denoted in the upper right. The dashed lines indicate the 1σ uncertainty on the linear ephemeris.

vary in phase with the orbital signal and a correlation in BS versus RV (Santos et al. 2002; Torres et al. 2005). The amplitude would be similar to that of the velocities (Queloz et al. 2001; Mandushev et al. 2005).

Following the prescription of Torres et al. (2005) and Torres et al. (2007), each APF spectrum was cross-correlated with a synthetic spectrum derived using the stellar properties determined from the high S/N Keck spectrum (see Section 3). We analyzed the cross-correlation function for each of the echelle orders between 4260 and 5000 Å in order to avoid the iodine lines and telluric lines. By restricting the BS analysis to blue orders, we reduce the effect of instrumental PSF variations caused by guiding errors because the seeing is degraded toward the blue, which means that the slit is more evenly illuminated. We measure the asymmetry in the spectral line profile for each order by calculating the velocity at the midpoint of lines connecting the CCF at many different fractional levels of CCF peak. The BS is then the difference in velocity between the 65th and 95th percentile levels of the CCF. The BS and error corresponding to a given observation are the mean and standard deviation on the mean over the 15 spectral orders analyzed.

Our BS measurements and errors are listed in Table 2 and shown in Figure 11. Figure 9 also shows the BS measurements as a function of orbital phase. We find no statistically significant correlation of BS with RV. The Spearman rank correlation coefficient is -0.35 ($p = 0.24$; Spearman 1904).

The lack of in-phase BS variations, and the fact that the stellar log g derived from spectroscopy and log g derived from the transit light curves are consistent to within 1σ lead us to conclude that the RV variations and transit signals are caused by a highly inflated Jovian planet.
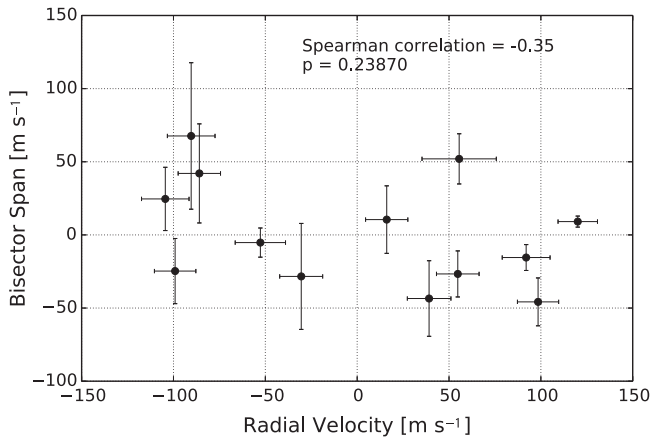
Figure 11. BS measurements for the APF spectra used for RV measurements. We find no significant correlation between RV and BS.

6. DISCUSSION

6.1. Prospects for Further Characterization of the Host Star

Further stellar characterization of KELT-8 is needed to better constrain the mass and radius of the star, which will improve our knowledge of the planetary mass and radius. Several more light curves with higher precision in which the two components are well-resolved would help to better constrain the stellar density. A more detailed analysis of higher S/N spectra may help to nail down the spectroscopically derived parameters and allow for chemical abundance measurements. *GAIA* (de Bruijne 2012) should provide a precise parallax to constrain the stellar luminosity and thus radius, and TESS and/or PLATO (Rauer et al. 2014) may provide sufficient photometric precision to measure the stellar density using asteroseismology.

6.2. Comparative Planetology

KELT-8b has the second largest radius of all known exoplanets, but has a mass slightly less than that of Jupiter. It lies well above the theoretical mass–radius curve for pure hydrogen (see Figure 12). KELT-8b is similar to WASP-1b (Collier Cameron et al. 2007) and HAT-P-41b (Hartman et al. 2012). It orbits a star more massive and metal-rich than the Sun ($M_\star \geqslant 1\,M_\odot$ and [Fe/H] $\geqslant 0.1$), the planet is highly irradiated ($a \leqslant 0.05$ AU), and it is less massive than Jupiter but still extremely inflated ($R_p \geqslant 1.5\ R_J$).

Next, we compare the stellar parameters of KELT-8 with other well-characterized hot Jupiter host stars. We use the exoplanets.org catalog to select the stars that host planets with orbital periods shorter than 10 days and masses between 0.4 and 1.1 M_J. We plot these stars on an HR diagram in Figure 13. We split this sample into two groups: one group containing the stars that host planets with radii greater than 1.5 R_J and the other containing stars that host planets smaller than 1.5 R_J. KELT-8 is the coolest star to host a highly inflated hot Jupiter ($T_{eff} = 5754$ K), but we find that all other stars that host similar highly inflated planets tend to be hotter than ≈ 5900 K. However, there are also plenty of stars hotter than 5900 K that host non-inflated hot Jupiters. We also compare stellar metallically, $v \sin i$, flux received by the planet, orbital eccentricity, stellar multiplicity, and spin–orbit misalignment, but find no clear differences between the hot stars that host "normal" hot Jupiters to those that host the highly inflated hot
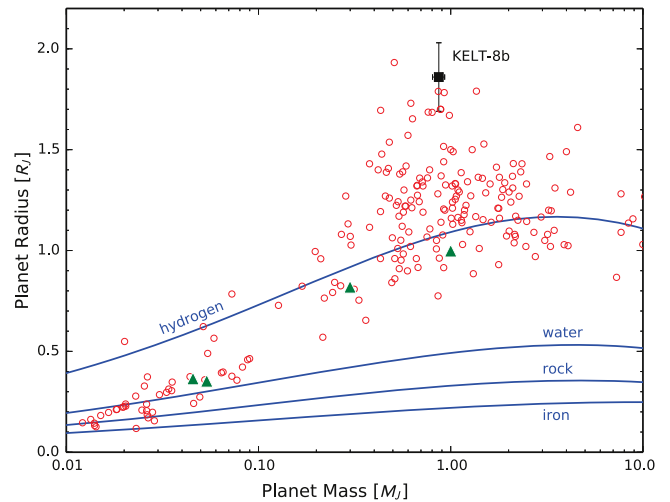

Figure 12. Mass-radius diagram of all confirmed transiting exoplanets (based on a 2015 February 17 query of exoplanets.org; red circles). KELT-8b is the annotated black square. Solar system planets are represented by green triangles. Model mass–radius relationships for idealized planets consisting of pure hydrogen, water, rock (Mg_2SiO_4), and iron are shown as blue lines (Seager et al. 2007). Only WASP-17b has a radius larger than the best-fit radius for KELT-8b.
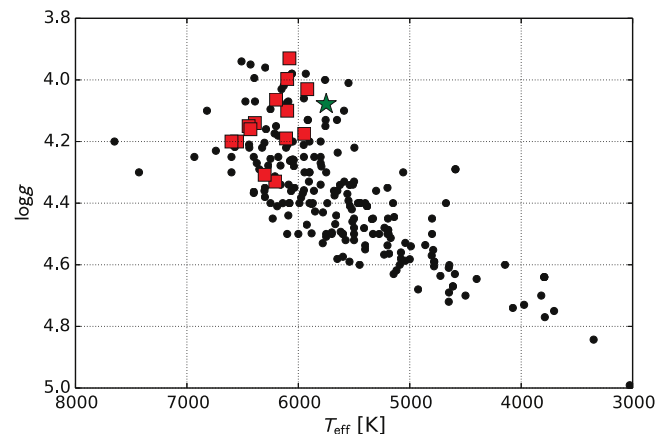

Figure 13. HR diagram showing well-characterized host stars of hot Jupiters. The red squares indicate stars that host planets with radii greater than 1.5 R_J, the green star marks the position of KELT-8, and the black circles are all other systems.

Jupiters with radii $\geqslant 1.5\ R_J$. However, we note that several of these host star parameters are poorly constrained for many of the systems. Albedo would be another interesting parameter to compare for these planets but it has not been measured for the majority of planets. It is possible that the highly inflated planets have abnormally low albedos and absorb more energy into their atmospheres at a given stellar insolation. TESS (Ricker et al. 2014) should provide light curves of sufficient precision to measure secondary eclipses in reflected light for most or all of these systems.

6.3. Mass–Radius Predictions

Several authors have identified empirical relations that attempt to predict the radius of a planet based on a combination of stellar and planetary properties. Enoch et al. (2012) established a relation that predicts planetary radius based only on the equilibrium temperature and orbital semimajor axis. KELT-8 falls into the Jupiter mass bin as defined by Enoch

et al. (2012) and the relation for that mass regime predicts a radius of 1.43 R_J, which is far too small relative to our measured value. The most recent empirical relation was presented by Weiss et al. (2013), which uses the incident flux and planetary mass as dependent variables. The Weiss et al. (2013) relation predicts a radius of 1.63 R_J for KELT-8. If one takes into account the scatter in the Weiss et al. (2013) relation (0.1 R_J), and the error on our radius measurement, the predicted and measured values agree to within 1.2σ.

6.4. Prospects for Atmospheric Characterziation

KELT-8 joins a rare breed of highly inflated hot Jupiters orbiting relatively bright stars. The extended atmosphere, combined with the large transit depth and bright apparent magnitude, makes KELT-8 one of the best targets for transmission spectroscopy. In addition, the large planetary radius and high equilibrium temperature give rise to a significant secondary eclipse depth. We calculate an expected eclipse depth of ≈ 1.3 mmag at 3.6 μm by taking the ratio of the blackbody emission from the planet to that of the star, and multiplying by $(R_P/R_*)^2$. A secondary eclipse of this depth would be easily accessible by *Spitzer*. Combining $T_{eq} = 1675$ from Table 4 with the planetary surface gravity of $\log g_P = 2.793$, we find that the scale height of a H_2-dominated atmosphere ($\mu_m = 2$) on KELT-8 would be $H = 1113$ km. This large scale height implies that the amplitude of a transmission spectroscopy signal would be $\frac{2R_P H}{R_*^2} = 0.22$ mmag (Winn 2010, assuming $H \ll R_P$). All of these calculations assume perfect heat redistribution and zero albedo for the planet. Studies of the atmospheric composition or temperature profile of KELT-8 may provide an explanation for its highly inflated radius.

6.5. Irradiation History

We have shown that KELT-8b is a highly inflated planet, joining the ranks of other hot Jupiters that manifest radii much larger than predicted by standard models for non-irradiated objects with Jovian masses. Several authors (e.g., Demory & Seager 2011) have suggested an empirical insolation threshold ($\approx 2 \times 10^8$ erg s^{-1} cm^{-2}) above which hot Jupiters exhibit increasing amounts of radius inflation. KELT-8b clearly lies above this threshold, with a current estimated insolation of $1.78^{+0.27}_{-0.22} 10^9$ erg s^{-1} cm^{-2}, and therefore its currently large inflated radius is not surprising. At the same time, the KELT-8 host star is found to currently be in a very rapid state of evolution, such that its radius is rapidly expanding as the star crosses the Hertzsprung gap toward the red giant branch. This means that the star's surface is rapidly encroaching on the planet, which presumably is rapidly driving up the planet's insolation as well as the rate of any tidal interactions between the planet and the star.

Therefore it is interesting to consider two questions: First, has KELT-8b's incident radiation from its host star been below the empirical radius inflation threshold in the past? If KELT-8b's insolation only recently exceeded the inflation threshold, the system could then serve as an empirical testbed for the different timescales predicted by different inflation mechanisms (see, e.g., Assef et al. 2009; Spiegel & Madhusudhan 2012). Second, what is the expected fate of the KELT-8b planet, given the increasingly strong tidal interactions it is experiencing with its encroaching host star?
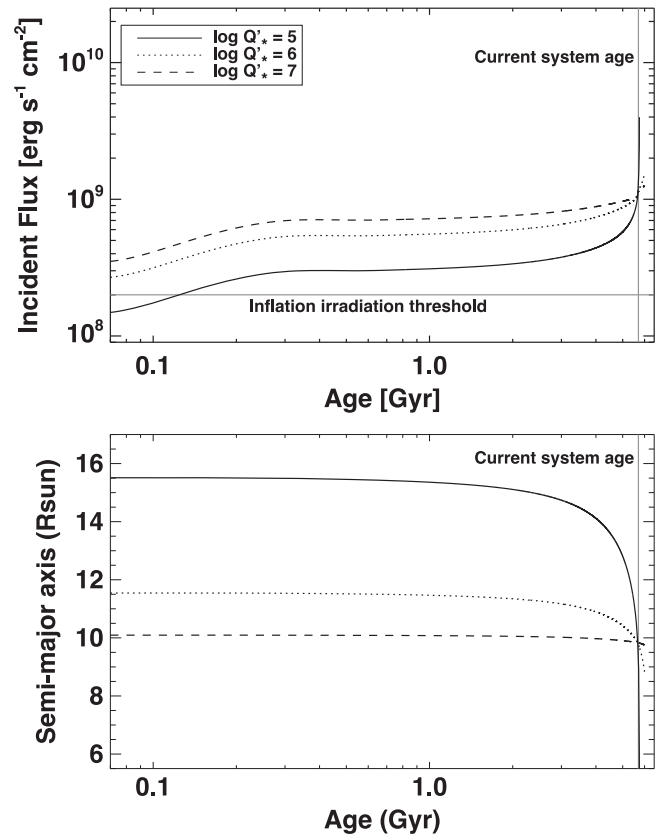

Figure 14. Top: irradiation history of KELT-8b. The insolation received by the planet is well above the empirical inflation irradiation threshold (Demory & Seager 2011) for the entire main-sequence existence of the star, except in the case of $\log Q'_\star = 5$ in the very early stages of stellar evolution. Bottom: orbital semimajor axis history of KELT-8b. The planet's semimajor axis is rapidly decreasing as the star evolves off the main sequence. It appears unlikely that KELT-8b will survive past the star's current subgiant phase.

To investigate these questions, we follow Penev et al. (2014) to simulate the reverse and forward evolution of the star–planet system, using the measured parameters listed in Tables 3 and 4 as the present-day boundary conditions. This analysis is not intended to examine any type of planet–planet or planet–disk migration effects. Rather, it is a way to investigate (1) the change in insolation of the planet over time due to the changing luminosity of the star and changing star–planet separation, and (2) the change in the planet's orbital semimajor axis due to the changing tidal torque as the star–planet separation changes with the evolving stellar radius. We include the evolution of the star, which is assumed to follow the Yonsei-Yale stellar model with mass and metallicity as in Table 4. For simplicity, we assume that the stellar rotation is negligible and treat the star as a solid body. We also assume a circular orbit aligned with the stellar equator throughout the full analysis. The results of our simulations are shown in Figure 14. We tested a range of values for the tidal quality factor of the star $Q'_\star$, from $\log Q'_\star = 5$ to $\log Q'_\star = 7$ (assuming a constant phase lag between the tidal bulge and the star–planet direction). $Q'_\star$ is defined as the tidal quality factor divided by the Love number ($Q'_\star = Q_\star/k_2$). We find that although for certain values of $Q'_\star$ the planet has moved substantially closer to its host during the past Gyr, in all cases the planet has always received more than enough flux from its host to keep the planet irradiated beyond the insolation threshold identified by Demory & Seager (2011),

except perhaps during the pre–main-sequence (prior to an age of ∼100 Myr).

Interestingly, the currently rapid evolution of the star suggests a concomitant rapid in-spiral of the planet over the next few 100 Myr, unless the stellar $Q'_\star$ is large. This planet therefore does not appear destined to survive beyond the star's current subgiant phase. As additional systems like KELT-8b are discovered and their evolution is investigated in detail, it will be interesting to examine the statistics of planet survival and to compare these to predictions such as those shown in Figure 14 to constrain mechanisms of planet-star interaction generally and the values of $Q'_\star$ specifically.

7. SUMMARY

We announce the discovery of the highly inflated hot Jupiter, KELT-8b. This planet was initially discovered in KELT photometry, then confirmed via high-precision follow-up light curves and RVs. We also present adaptive optics imaging of KELT-8 from the Robo-AO system. Astrometry measurements over the past 110 years combined with high-resolution spectra of both components firmly establishes the visual companion at 8″.8 separation as an unrelated background star.

We develop a new technique to extract reliable RVs from noisy data that saves a significant amount of telescope time. In the case of RV follow-up for the confirmation or mass measurements of transiting planets where the ephemeris is known and only a few well-timed RV measurements are needed, this technique can save 30%–50% of the time by avoiding the need to collect a high quality iodine-free template observation. In addition, lower S/N is required for the RV measurement observations (S/N ≈ 50) through the iodine cell because one component of our model is now completely noise free. Normally, we collect S/N = 200 for our precision RV exposures using the standard observed template technique.

KELT-8b has one of the largest radii of any known transiting planet with $R_P = 1.86^{+0.18}_{-0.16}\ R_J$. It joins a small and interesting class of highly inflated hot Jupiters orbiting stars slightly more massive than the Sun.

REFERENCES

Alard, C. 2000, A&AS, 144, 363
Alard, C., & Lupton, R. H. 1998, ApJ, 503, 325
Albrecht, S., Winn, J. N., Johnson, J. A., et al. 2012, ApJ, 757, 18
Assef, R. J., Gaudi, B. S., & Stanek, K. Z. 2009, ApJ, 701, 1616
Bailey, J. I., III, White, R. J., Blake, C. H., et al. 2012, ApJ, 749, 16
Bakos, G. Á., Kovács, G., Torres, G., et al. 2007, ApJ, 670, 826
Baraffe, I., Chabrier, G., Allard, F., & Hauschildt, P. H. 2002, A&A, 382, 563
Baranec, C., Riddle, R., Law, N. M., et al. 2013, Journal of Visualized Experiments, 72, e50021
Baranec, C., et al. 2014, ApJL, 790, L8
Batygin, K., Stevenson, D. J., & Bodenheimer, P. H. 2011, ApJ, 738, 1
Bayliss, D. D. R., & Sackett, P. D. 2011, ApJ, 743, 103
Beatty, T. G., Pepper, J., Siverd, R. J., et al. 2012, ApJL, 756, L39
Bensby, T., Feltzing, S., & Lundström, I. 2003, A&A, 410, 527
Bento, J., Wheatley, P. J., Copperwheat, C. M., et al. 2014, MNRAS, 437, 1511
Bianchi, L., Herald, J., Efremova, B., et al. 2011, Ap&SS, 335, 161
Bieryla, A., Collins, K., Beatty, T. G., et al. 2015, AJ, 150, 12
Burt, J., Vogt, S. S., Butler, R. P., et al. 2014, ApJ, 789, 114
Butler, R. P., Marcy, G. W., Williams, E., et al. 1996, PASP, 108, 500
Chubak, C., Marcy, G., Fischer, D. A., et al. 2012, arXiv:1207.6212
Coelho, P. R. T. 2014, MNRAS, 440, 1027
Collier Cameron, A., Bouchy, F., Hébrard, G., et al. 2007, MNRAS, 375, 951
Collins, K. A., Eastman, J. D., Beatty, T. G., et al. 2014, AJ, 147, 39
Cumming, A., Butler, R. P., Marcy, G. W., et al. 2008, PASP, 120, 531
Cutri, R. M., Skrutskie, M. F., van Dyk, S., et al. 2003, yCat, 2246, 0
Cutri, R. M., Wright, E. L., Conrow, T., et al. 2014, yCat, 2328, 0
Dawson, R. I. 2014, ApJL, 790, L31
Dawson, R. I., & Murray-Clay, R. A. 2013, ApJL, 767, L24
de Bruijne, J. H. J. 2012, Ap&SS, 341, 31
Demory, B.-O., & Seager, S. 2011, ApJS, 197, 12
Eastman, J., Gaudi, B. S., & Agol, E. 2013, PASP, 125, 83
Enoch, B., Collier Cameron, A., & Horne, K. 2012, A&A, 540, A99
Fulton, B. J., Shporer, A., Winn, J. N., et al. 2011, AJ, 142, 84
Fulton, B. J., Howard, A. W., Winn, J. N., et al. 2013, ApJ, 772, 80
Gellera, D. 1984, DSSC, 3, 3
Gellera, D. 1990, AN, 311, 117
Ginzburg, S., & Sari, R. 2015, ApJ, 803, 111
Gould, A., Dorsher, S., Gaudi, B. S., & Udalski, A. 2006, AcA, 56, 1
Hansen, B. M. S., & Murray, N. 2012, ApJ, 751, 158
Hartkopf, W. I., Mason, B. D., Finch, C. T., et al. 2013a, AJ, 146, 76
Hartkopf, W. I., Mason, B. D., Finch, C. T., et al. 2013b, AJ, 146, 76
Hartman, J. D., Bakos, G. Á., Béky, B., et al. 2012, AJ, 144, 139
Hirano, T., Suto, Y., Winn, J. N., et al. 2011, ApJ, 742, 69
Høg, E., Fabricius, C., Makarov, V. V., et al. 2000, A&A, 355, L27
Howard, A. W., Marcy, G. W., Bryson, S. T., et al. 2012, ApJS, 201, 15
Huber, D., Ireland, M. J., Bedding, T. R., et al. 2012, ApJ, 760, 32
Ida, S., & Lin, D. N. C. 2008, ApJ, 673, 487
Ivezić, Ž, Beers, T. C., & Jurić, M. 2012, ARA&A, 50, 251
Jensen, E. 2013, ascl soft, ascl:1306.007
Johnson, J. A., Marcy, G. W., Fischer, D. A., et al. 2006, ApJ, 647, 600
Joshi, Y. C., Pollacco, D., Collier Cameron, A., et al. 2009, MNRAS, 392, 1532
Kharchenko, N. V. 2001, KFNT, 17, 409
Kipping, D. M., Hartman, J., Bakos, G. Á., et al. 2011, AJ, 142, 95
Knutson, H. A., Fulton, B. J., Montet, B. T., et al. 2014, ApJ, 785, 126
Kovács, G., Bakos, G., & Noyes, R. W. 2005, MNRAS, 356, 557
Kurucz, R. L. 1979, ApJS, 40, 1

Law, N. M., Morton, T., Baranec, C., et al. 2014, ApJ, 791, 35
Lockwood, A. C., Johnson, J. A., Bender, C. F., et al. 2014, ApJL, 783, L29
Lucy, L. B., & Sweeney, M. A. 1971, AJ, 76, 544
Mandushev, G., Torres, G., Latham, D. W., et al. 2005, ApJ, 621, 1061
Marcy, G. W., & Butler, R. P. 1992, PASP, 104, 270
Mordasini, C., Alibert, Y., & Benz, W. 2009, A&A, 501, 1139
Ngo, H., Knutson, H. A., Hinkley, S., et al. 2015, ApJ, 800, 138
Penev, K., Zhang, M., & Jackson, B. 2014, PASP, 126, 553
Pepper, J., Pogge, R. W., DePoy, D. L., et al. 2007, PASP, 119, 923
Pepper, J., Siverd, R. J., Beatty, T. G., et al. 2013, ApJ, 773, 64
Pickles, A., & Depagne, É 2010, PASP, 122, 1437
Pourteau, M. A. 1933, Observatoire de Paris. Catalogue des étoiles doubles de la zone + 24° de la carte photographique du ciel (Orléans: impr. de H. Tessier)
Queloz, D., Henry, G. W., Sivan, J. P., et al. 2001, A&A, 379, 279
Radovan, M. V., Lanclos, K., Holden, B. P., et al. 2014, Proc. SPIE, 9145, 2
Rauer, H., Catala, C., Aerts, C., et al. 2014, ExA, 38, 249
Ricker, G. R., Winn, J. N., Vanderspek, R., et al. 2014, Proc. SPIE, 9143, 20
Santos, N. C., Mayor, M., Naef, D., et al. 2002, A&A, 392, 215
Seager, S., Kuchner, M., Hier-Majumder, C. A., & Militzer, B. 2007, ApJ, 669, 1279
Sing, D. K., Wakeford, H. R., Showman, A. P., et al. 2015, MNRAS, 446, 2428
Siverd, R. J., Beatty, T. G., Pepper, J., et al. 2012, ApJ, 761, 123
Snellen, I. A. G., Brandl, B. R., de Kok, R. J., et al. 2014, Natur, 509, 63
Southworth, J., Hinse, T. C., Dominik, M., et al. 2012, MNRAS, 426, 1338
Spearman, C. 1904, The American Journal of Psychology, 15, 72
Spiegel, D. S., & Madhusudhan, N. 2012, ApJ, 756, 132
Stetson, P. B. 1987, PASP, 99, 191
Stetson, P. B. 1990, PASP, 102, 932
Tanner, A., White, R., Bailey, J., et al. 2012, ApJS, 203, 10
Ter Braak, C. 2006, Statistics and Computing
Torres, G., Andersen, J., & Giménez, A. 2010, A&Ar, 18, 67
Torres, G., Konacki, M., Sasselov, D. D., & Jha, S. 2005, ApJ, 619, 558
Torres, G., Bakos, G. Á., Kovács, G., et al. 2007, ApJL, 666, L121
Valenti, J. A., & Fischer, D. A. 2005, ApJS, 159, 141
Vogt, S. S., Allen, S. L., Bigelow, B. C., et al. 1994, Proc. SPIE, 2198, 362
Vogt, S. S., Radovan, M., Kibrick, R., et al. 2014, PASP, 126, 359
Weiss, L. M., Marcy, G. W., Rowe, J. F., et al. 2013, ApJ, 768, 14
Winn, J. N. 2010, arXiv:1001.2010
Winn, J. N., Johnson, J. A., Fabrycky, D., et al. 2009, ApJ, 700, 302
Wright, J. T., Marcy, G. W., Howard, A. W., et al. 2012, ApJ, 753, 160
Zhao, M., O'Rourke, J. G., Wright, J. T., et al. 2014, ApJ, 796, 115